Monthly Notices
of the
ROYAL ASTRONOMICAL SOCIETY

MNRAS **482,** 5023–5040 (2019)
Advance Access publication 2018 November 10

doi:10.1093/mnras/sty3029

SPLOT: a snapshot survey for polarized light in optical transients

A. B. Higgins [1]★ K. Wiersema,[1,2] S. Covino [3] R. L. C. Starling,[1] H. F. Stevance [4] Ł. Wyrzykowski,[5] S. T. Hodgkin,[6] J. R. Maund [4] P. T. O'Brien[1] and N. R. Tanvir[1]

[1]*Department of Physics and Astronomy, University of Leicester, University Road, Leicester LE1 7RH, UK*
[2]*Department of Physics, University of Warwick, Coventry CV4 7AL, UK*
[3]*INAF/Brera Astronomical Observatory, via Bianchi 46, I-23807, Merate (LC), Italy*
[4]*Department of Physics and Astronomy, University of Sheffield, Hounsfield Rd, Sheffield S3 7RH, UK*
[5]*Warsaw University Astronomical Observatory, Al. Ujazdowskie 4, PL-00-478 Warszawa, Poland*
[6]*Institute of Astronomy, University of Cambridge, Madingley Road, Cambridge CB3 0HA, UK*

Accepted 2018 November 3. Received 2018 October 5; in original form 2018 July 13

ABSTRACT

We present SPLOT, a small-scale pilot survey to test the potential of snapshot (single epoch) linear imaging polarimetry as a supplementary tool to traditional transient follow-up. Transients exist in a vast volume of observational parameter space and polarimetry has the potential to highlight sources of scientific interest and add value to near real-time transient survey streams. We observed a sample of ∼50 randomly selected optical transients with the EFOSC2 (ESO Faint Object Spectrograph and Camera v2) and SofI (Son of ISAAC) instruments, on the 3.6 m New Technology Telescope to test the feasibility of the survey. Our sample contained a number of interesting individual sources: a variety of supernovae, X-ray binaries, a tidal disruption event, blazar outbursts and, by design, numerous transients of unknown nature. We discuss the results, both for the individual sources and the survey in detail. We provide an overview on the success and limitations of SPLOT and also describe a novel calibration method for removing instrumental polarization effects from Nasymth-mounted telescopes. We find that a SPLOT-like survey would be a benefit to the large-scale future transient survey streams such as Large Synoptic Survey Telescope. The polarimetric measurements have added scientific value to a significant number of the sources and, most importantly, have shown the potential to highlight unclassified transient sources of scientific interest for further study.

Key words: polarization – supernovae: general – galaxies: active.

1 INTRODUCTION

The discovery space of transients now spans an unprecedented range of wavelengths and time-scales, continuously pushed by new campaigns and software and, as a result, the rate of transient candidate discovery has increased dramatically in recent years. There are a number of current facilities whose aim it is to detect a variety of transient phenomena including the Mobile Astronomical System of Telescope-Robots (MASTER; Lipunov et al. 2004), the All Sky Automated Survey for SuperNovae (ASAS-SN; Shappee et al. 2014), the *Gaia* satellite (Gaia Collaboration et al. 2016), the Panoramic Survey Telescope and Rapid Response System (Pan-STARRS; Chambers et al. 2016), and the Optical Gravitational Lensing Experiment (OGLE) IV Transient Detection System (Wyrzykowski et al. 2014) to name a few. The current number of detections from optical transient surveys lies at ∼1–10 transients per night. At optical wavelengths, large additional increases in discovery rates are expected from the arrival of new surveys such as the Large Synoptic Survey Telescope (LSST; Ivezic et al. 2008) and the Gravitational-Wave Optical Transient Observer.[1] Moreover, the Zwicky Transient Facility (ZTF; Kulkarni 2016) has also recently become operational and has been distributing alerts to the transient community since 2018 June. In many cases, the discovery data and subsequent photometry provided by these surveys alone do not provide enough information to accurately filter the targets of highest astrophysical interest from the streams and follow-up data are required. Traditionally, the key follow-up resource is spectroscopy, but spectroscopic observations are usually time expensive and cannot feasibly be used on large volumes of transients.

An important primary step is therefore the ability to filter and choose interesting transient sources in near real time directly from incoming data streams. The classification of new transient sources via follow-up spectroscopic observations is well studied by large

★ E-mail: abh13@le.ac.uk

[1]https://goto-observatory.org/

programmes (i.e. Public ESO Spectroscopic Survey of Transient Objects; PESSTO, Smartt et al. 2015) . However, there is a large number of potentially interesting, transient-enabled astrophysics that does not map cleanly onto selection functions based on multi-wavelength flux (ratios), astrometric position, morphology, or low-resolution spectroscopic features – particularly with selection functions that are available early after alert. Linear polarimetry may go some way towards providing an additional observational parameter axis for large numbers of transients with the potential to flag up astrophysics of interest.

Many high-energy astrophysical phenomena have complex internal geometry. Intrinsic linear polarization of the order of several per cent can help decipher the complex geometry and magnetic field configuration of regions with optical emission. Optical linear polarization can arise from a number of mechanisms. The presence of non-thermal emission in the form of synchrotron emission, produced by relativistic electrons gyrating around magnetic field lines and thought to arise in a host of transient phenomena, exhibits a significant level of polarization. This emission mechanism is thought to dominate the low-energy (optical to radio) photon production in active galactic nucleus (AGN)/Blazars (Trippe 2014), the emission from X-ray to radio wavelengths in Gamma-ray Burst (GRB) afterglows (Wiersema et al. 2012b, 2014; Covino & Gotz 2016), and X-ray binary (XRB) jets (Russell & Fender 2008) to name a few. For core-collapse supernovae (SNe) a non-zero measurement of polarization arises from asymmetric explosion ejecta (Shapiro & Sutherland 1982; Wang, Wheeler & Höflich 1997; Wang & Wheeler 2008) and additionally can arise from inhomogeneous ejecta in novae outbursts (Evans et al. 2002). Type Ia SNe observations have shown that the intrinsic continuum light shows no significant levels of polarization (Wang et al. 1996; Wang et al. 1997; Wang & Wheeler 2008). However, multiple detections of significant polarization have been detected in broad-band optical filters (i.e. SN2014J; Kawabata et al. 2014). Polarization of this nature has been attributed to line-of-sight dust, potentially in the SN host, giving us a window into the immediate environment of the source.

We have undertaken a pilot study measuring the optical linear polarization of a variety of high-energy transients and variables through single epoch polarimetry. We highlight the aims, use and justification of undertaking a polarimetric survey and introduce our observations in Section 2. We discuss our polarimetric data analysis, calibration efforts and measurements in Section 3 and our photometry in Section 4. Section 5 showcases the main results of SPLOT. We discuss the impact of the survey and the shape of future polarimetric surveys in Section 6.

2 OBSERVATIONS

2.1 Survey rationale

The main aim of this survey was to investigate the opportunities and practicalities of using a snapshot linear polarization measurement survey as a tool to add value to streams of optical transients. In particular, we aimed to explore whether polarization alone could allow us to highlight transient sources of high scientific interest, independent of the traditional classification tools of light curves and spectra. As discussed in the introduction, astrophysical transients can exhibit significant and varying levels of intrinsic linear polarization based on their internal structure and equally wide range due to dust in the environment of the source. These transient events cover a large range of both absolute magnitudes and physical time-scales (see Fig. 1) resulting in a large polarimetric parameter space. If you include additional observational parameters such as multiwavelength follow-up, colours and potential host information, transients cover a vast multidimensional space. Value can be added onto survey transient streams by mapping out where sources fit into this multidimensional parameter set and hence highlight any sources of scientific interest. Spectral classification, while crucially important to many aspects of transient science, may not highlight all sources of interest and we therefore want to test linear optical polarimetry as an independent aid of large-scale transient streams.

Linear optical polarimetry has been a fairly standard tool in the follow-up of some transients, in particular SN (Wang & Wheeler 2008) where optical spectropolarimetry has provided constraints on SNe geometry (i.e. Maund et al. 2009; Reilly et al. 2017; Stevance et al. 2017). SN rates are high enough that such a pre-selection can be made well, and a reasonable number of sources are available for spectropolarimetry. For many other transient classes, only a very small number of sources have follow-up polarimetry (i.e. Macronova; Covino et al. 2017). These uncommon transients typically have a low rate of detection and may be considerably fainter. As we also aimed to observe a relatively large sample of sources we therefore opted for broad-band imaging polarimetry which requires substantially shorter exposure times than spectropolarimetry.

To investigate the feasibility of our survey we required a relatively large sample of sources to:

(i) Sample both the contents of transient survey streams and a broad area of the discussed parameter space.
(ii) Cover the effects of Galactic dust induced polarization.
(iii) Investigate the effect of practical constraints such as weather, instrument calibration, and ease of access to transient alerts by surveys.
(iv) Obtain results to sufficient precision that to enable scientific conclusions on individual sources ($\sigma_P \sim 0.2$ per cent).

To achieve this we chose a snapshot approach where the majority of sources are observed just once, in a single broad-band filter. Detailed studies of some source classes in the literature can then be used to place selected single sources into context. A small subset of sources is observed more than once, generally as a test of calibration fidelity and occasionally to assess polarimetric variability over short time-scales or multiwavelength behaviour.

2.2 Source selection, exposure times, and impact of conditions

2.2.1 Telescope, instrumental set-up, and filter choice

The rate of transients is currently sufficiently high that it is feasible to use ‘ visitor-mode’ observing to perform a survey like SPLOT, as demonstrated by the success of the ePESSTO[2] (Smartt et al. 2015) SN survey.

We required the use of a medium-sized telescope (∼4 m) with an execution time of 1 h or less per target to fulfill the following criteria:

(i) Cover a magnitude range down to ∼20 mag in *V*- band – where more uncommon (extragalactic) transients typically appear (see Fig. 1; Rau et al. 2009).

[2] http://www.pessto.org

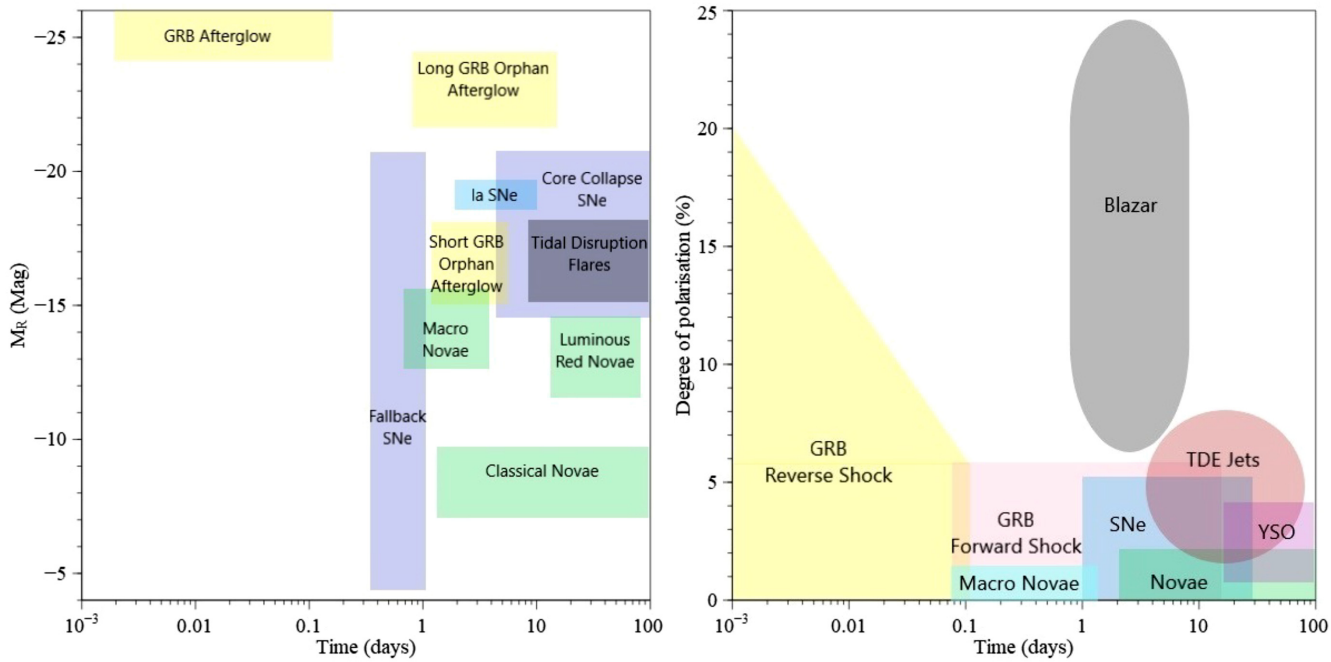

Figure 1. Left: absolute magnitude and characteristic time-scales for a range of optical transients, demonstrating the large area of discovery space of optically selected transient searches in the light-curve domain – similar layout to fig. 8.1 in LSST Science Collaboration et al. (2009). Right: discovery space of SPLOT, in the optical polarimetric domain. The *x*-axis represents a characteristic time-scale. Indicated are approximate regions where some polarimetric detections exist – not necessarily intrinsic polarization. Current statistics are very poor for some of the discovery space: several of the source classes have just one or two polarimetric measurements.

(ii) Aim for polarimetric uncertainties of ∼0.2 per cent with ∼0.5 per cent for the faintest sources. In reality, the dominant source of uncertainty will be weather conditions and instrumental effects.

(iii) Observe a fairly large (∼50) sample of transients.

For the survey we used the ESO 3.6 m New Technology Telescope (NTT) at La Silla, Chile, primarily with the ESO Faint Object Spectrograph and Camera v2 (EFOSC2; Buzzoni et al. 1984). This instrument is widely used for transient observations (i.e. ePESSTO), has the ability to switch rapidly from imaging to imaging polarimetry, and offers a field of view (FOV) well suited for transient follow-up (see ESO 2016a for full details). In addition to EFOSC2, some observations were obtained using the infrared instrument SofI (Son of ISAAC; Moorwood, Cuby & Lidman 1998) which is also capable of performing polarimetric observations (see ESO 2016b for full details). We note that both instruments exhibit large amounts of instrumental polarization since they are both located at the Nasmyth focus (see Section 3.2 for full discussion).

For the primary snapshot survey, we choose to use the *V* filter for EFOSC2 observations. It overlaps well with the *Gaia* passband and that of ASAS-SN and MASTER, making it easier to extrapolate discovery magnitudes to the time of observation. Furthermore, the efficiency of EFOSC2 peaks near the *V* band and we avoid systematics from fringing by not choosing redder filters. The observed polarization we measure is a combination of three contributors: the intrinsic polarization of the target source, the polarization induced by *in situ* dust scattering and the induced polarization from dust within the Milky Way. The *V* band is close to the wavelength at which the dust induced polarization peaks in the Milky Way (e.g. Serkowski, Mathewson & Ford 1975). As such, we may not be able to separate the Galactic dust component from the intrinsic one using just a single snapshot in one filter. However, this allows us to use dust as an additional parameter of interest. For the SofI observations we used the *Z* filter, to stay as close as possible to the optical bands used by the transient feed surveys.

2.2.2 *Chosen targets*

We selected the SPLOT targets from a number of transient surveys that release rapid public notifications; generally through the Transient Name Server,[3] on survey specific web-based lists[4] and/or via announcements in Astronomers Telegrams[5] and VOEvents.[6] The main contributors to the source list were the *Gaia* transient alert system, PanSTARRS, ASAS-SN, ATLAS, MASTER, CRTS, OGLE and some other, smaller streams. We deliberately did not require prior spectroscopic classification for an object to enter our list of possible targets. The main requirement for a transient to become a target was its visibility ($\gtrsim$ 0.5h at airmass < 2) from La Silla observatory in our observing nights. Targets for which an alert was received within six months were entered into our target list granting us coverage of our target discovery space. Many targets received further observations since discovery and sources that had faded below magnitude ∼21 were culled from the target list.

During observing nights the transient feed surveys were checked continuously for new transients – we note that the *Gaia* transient

[3] https://wis-tns.weizmann.ac.il
[4] e.g. http://gsaweb.ast.cam.ac.uk/alerts/home
[5] http://www.astronomerstelegram.org
[6] We use the Comet broker (Swinbank 2014), https://github.com/jdswinbank/Comet

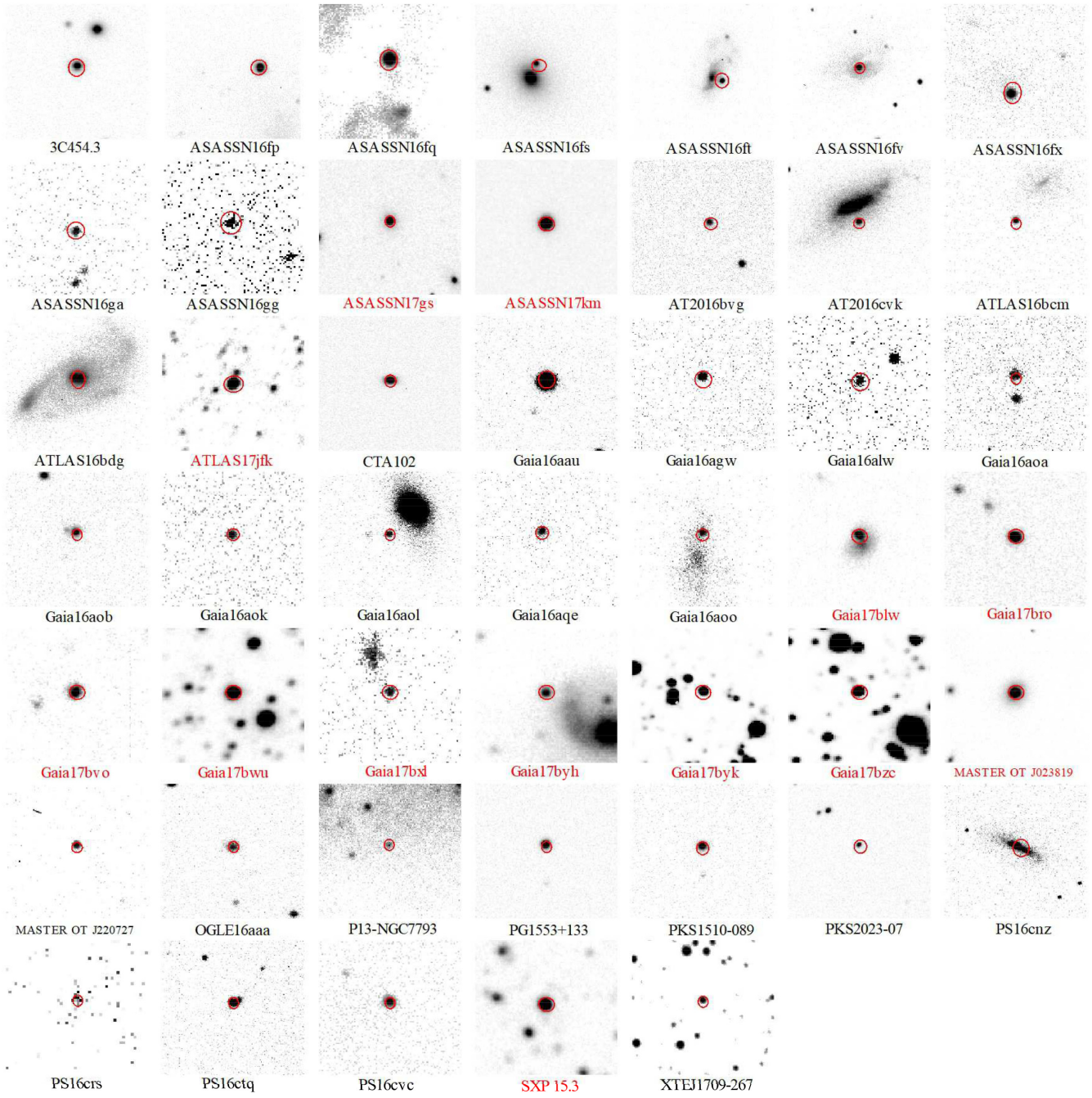

Figure 2. Images of the sources that we observed as part of SPLOT. The image for GX304-1 was saturated and therefore not included. The images are purely used as a reference for the position of each source within their hosts and/or neighbouring field stars, and are not to scale. Images were taken in *V*- band (EFOSC2; black text) or *Z*- band (SofI; red text).

alert system was off during our first run in 2016 resulting in the more frequent use of older transients – with earlier discovery dates. The full target list was ingested into *iObserve*,[7] from which altitude, Moon distance, and parallactic angle (PA) were obtained. We then used these observables to create an observing plan. Instrumental polarization of these instruments is strongly dependent on PA so observations were planned near times when PA changes were small over the observation execution time. ESO observing blocks (OBs) were created as new alerts came in during the observing nights and a set of reserve targets (older transients) were prepared a night in advance in case of a lack of new transients or highly adverse weather. Exposure times were changed in cases where acquisition images showed a flux strongly different from expectations.

Additional criteria had to be introduced at periods of poor weather. Poor seeing and cloud coverage made observing the faintest sources very challenging. Several nights suffered from strong winds from the North, which meant that only objects towards the South (typically with declination $\lesssim -30^{\circ}$) could be observed. This di-

[7] onekilopars.ec

rectly impacted survey source selection with some surveys (i.e. PanSTARRS and the Asteroid Terrestrial-impact Last Alert System; ATLAS) unable to provide transients at low declinations. Additionally, photometric follow-up of transients is more sparse at low declinations making it harder to estimate exposure times for SPLOT observations.

Overall, we observed 47 optical transients and an additional eight standard stars – three polarized and five unpolarized. Images of the transients are shown in Fig. 2.

2.3 La Silla data acquisition

The majority of our targets were observed with EFOSC2, primarily using the *V* filter (ESO filter no. 641). We obtained our data during three observation nights (2016 June 19, 20, and 22), under poor seeing and variable thin to thick cloud conditions. Two further allocated nights (June 23 and 24) were fully lost to thick cloud and high humidity. The Moon was near full throughout. Sources were additionally observed with the *B* and *R* filters in selected cases (ESO filters nos 639 and 642, respectively). A second block of NTT EFOSC2 observing time was awarded for SPLOT. However, the rotator encoder of the Nasmyth platform on which EFOSC2 was mounted failed, and could not be repaired on time. We therefore used SofI instead, which is mounted on the opposite Nasmyth platform, and chose to use the *Z* filter. Science observations were obtained on the first two nights (2017 August 7 and 8), under variable cloud and poor seeing. The third night (August 9) was lost to cloud and humidity.

2.3.1 *EFOSC2 data*

Our EFOSC2 polarimetric observations used a Wollaston prism ('Woll_Prism20') and a half-wave plate. The prism was used to split the incoming light into two beams, the orthogonally polarized ordinary (*o*) and extraordinary (*e*) beams. A mask was used to ensure the images of the two beams do not overlap (Fig. 3). We used four different half-wave plate angles for our observations; 0°, 22.5°, 45°, and 67.5°. The use of four angles instead of two angles allows us to obtain superior accuracy for our polarimetric measurements through beam switching (Patat & Romaniello 2006), as discussed in Section 3.1. We obtained dome screen flat field images with the polarimetric elements in place, with the half-wave plate rotating continuously to form a flat field where polarization response is scrambled. Bias frames were also taken at the start of each night. The CCD readout was in 'normal' mode and used 2 × 2 binning, resulting in an image scale of 0.24 arcsec pixel^{-1}. The gain and read noise of the CCD in this mode were 1.18 electrons per ADU and 11 electrons respectively, calculated using the method described in Janesick (2001). As EFOSC2 is mounted on a Nasmyth platform, light reflects off of a mirror set at a 45° angle with respect to EFOSC2 (the tertiary mirror). This leads to significant levels of instrumental polarization (Giro et al. 2003) discussed further in Section 3.1. To minimize part of this instrumental polarization, we always placed the transients and standard stars at (nearly) the same pixel position as part of the acquisition process (Fig. 3).

Once exposures at all four half-wave plate positions had been completed, the images were reduced using standard IRAF[8] tasks, and the IRAF task APPOLA[9] was used to measure fluxes in the *o* and *e* images in each frame, using aperture photometry. A circular shaped extraction region, typically 1.5 times the full width at half-maximum (FWHM) of the point spread function (PSF), was used to obtain the fluxes of the sources (f_o and f_e). An annulus shaped sky region, with inner radius typically three times the FWHM, was used for the surrounding background region. Sky annuli were occasionally tweaked to avoid nearby field stars. This procedure was carried out for all point sources in the images. We ensured aperture size and annuli sizes were fixed for each of the four half-wave plate angles making up one observation. For a more detailed description, see Rol et al. (2003). Output files were created for each half-wave plate angle observation and we created a pipeline written in PYTHON3.5[10] to parse output files, calibrate the instrumental polarization, and calculate the polarization of all sources (Wiersema et al. 2018; method and calibration of results discussed in Section 3).

Because of the aperture mask, which blocks half the field in strips (Fig. 3), there are frequently not many field stars present in the polarimetry data. To perform photometry on each source, we therefore acquired a short exposure image in the *V* band, directly after the four half-wave plate rotations. We used twilight flats and bias frames to reduce these data, using standard IRAF tasks. A further pipeline was produced to calculate the brightness of each source (discussed in Section 4).

2.3.2 *SofI data*

SofI also uses a Wollaston prism to split the light into two orthogonally polarized beams, and a mask to avoid image overlap (Fig. 3). In contrast to EFOSC2, SofI has no wave plates, which means the Wollaston prism needs to be rotated with respect to the detector to acquire the Stokes parameters. We rotated the instrument through four angles: 0°, 45°, 90°, and 135° – equivalent to rotating a wave plate through the four angles described in Section 2.3.1.

As SofI is an infrared instrument, its observing setup is slightly different from EFOSC2. Each observation at one angle consists of an exposure time NEXP × NDIT × DIT, where DIT is the detector integration time in seconds, NDIT the number of DIT integrations that is averaged to make a single output file and NEXP the number of separate NDIT × DIT files. Small dithers are applied between each (NDIT × DIT) set, typically a few arcseconds. We always used an NEXP of five for the polarimetric exposures. We chose the dithers and the pixel coordinate on which the source was placed (in the acquisition template) such that the transient always stayed in the central area of the mask. The chosen NEXP × NDIT × DIT for each source is listed in Table 2. We note that at the time of observations no exposure time calculator for the SofI *Z* band imaging existed so exposure times were estimated on the fly using acquisition data. SofI uses a Hawaii HgCdTe array, with pixel scale of 0.288 arcsec pixel^{-1} in its wide-field mode. To reduce the data we acquired dark frames at the start of the nights with a variety of DIT × NDIT to match the science and standard star observations. Flat field exposures were obtained using the 'Special Flat' dome flat algorithm described in the Sofi manual (ESO 2016b), note that these were obtained without polarization optics (Wollaston) in the beam: unlike EFOSC2, there

[8] IRAF (Image Reduction and Analysis Facility) is distributed by the National Optical Astronomy Observatories, which are operated by the Association of Universities for Research in Astronomy, Inc., under cooperative agreement with the National Science Foundation.

[9] Developed by E. Rol

[10] http://www.python.org

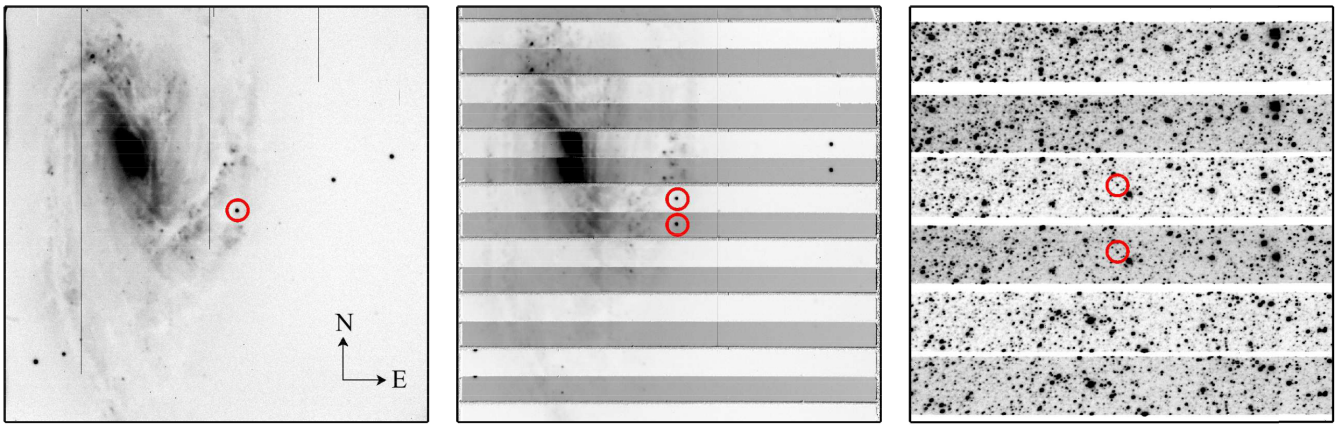

Figure 3. The three panels show from left to right: a *V*-band EFOSC2 image of ASASSN-16fq (an example of a transient on a bright galaxy background), the same source in a single exposure of the EFOSC2 *V*-band polarimetric sequence and a single SofI *Z*-band exposure from a polarimetric sequence of Gaia17bzc (an example of a transient in a crowded field). The transient is indicated with a red circle and the orientation of EFOSC2 is indicated with a compass. The SofI orientation is different from EFOSC2 (East down, North left at zero instrument rotation), and the field is rotated within the polarimetric sequence (see Section 2.3.2). The strips of the mask are clearly visible in the polarimetry images.

is no wave plate to spin continuously while taking these dome flats. The flat fields were processed using IRAF task FLAT_SPECIAL[11]. The science and standard star exposures were reduced using IRAF tasks, and the NEXP images (of one rotation angle for one source) were registered on a common pixel grid and combined using an average. The sky background in *Z*-band is far lower than that in the *J,H,K* bands so we do not perform sky subtraction steps used in most IR reduction. We do not perform corrections for interquadrant row cross talk in the polarimetry data: in none of the data does this effect play a role near the transient location. During SofI observations there were intermittent problems with the detector electronics making some quadrants in some NDIT × DIT exposures highly noisy and stripy. Manual intervention in the instrument ensured only a few frames were affected, these were eliminated from the averages. The resulting average frames at four angles were analysed in the same way as the EFOSC2 data, using aperture photometry.

As with EFOSC2 we obtained SofI imaging data of the targets. These consist of fewer NDIT and NEXP (generally three successive images were taken with NDIT = NEXP = 1) and therefore still show some noise residuals (e.g. from the amplifier) after reduction using dark and flat field frames. Row-by-row sky subtraction satisfactorily removed most of these. Images were further analysed in the same way as the EFOSC2 images.

2.4 Oadby data acquisition

To get a somewhat longer time-scale view of the light-curve properties of a small number of the SPLOT transients we observed a small subset using the University of Leicester 0.5 m telescope (UL50).[12] The telescope is a Planewave CDK20,[13] a 0.5m telescope of corrected Dall-Kirkham design. We used SBIG ST2000XM and Moravian G3-11000 CCD cameras equipped with a broad-band Johnson–Cousins *B,V,R,I* filter set. Bias, dark, and twilight (or dome) flat frames were obtained each observing night and data were reduced using standard recipes through a dedicated IRAF pipeline for UL50 data.

3 MEASURING SOURCE POLARIZATION

3.1 Data analysis

We represent our polarization results as a Stokes vector, taking the form $[S] = [I, Q, U, V]$ where I represents the intensity, Q and U express the linear polarization and V represents the circular polarization (described in Chandrasekhar 1960 and references therein). We do not measure circular polarization for this investigation. When calculating our polarimetric results we use the normalized Stokes parameters $q = Q/I$ and $u = U/I$. As mentioned in Section 2.3 using four rotation angles allows us to obtain smaller uncertainties on our measurements by cancelling out systematics effects caused by background subtraction and flat fielding (Patat & Romaniello 2006).

To calculate the observed values of q and u we first find the normalized flux difference, $F_{\rm i}$, between the ordinary and extraordinary beams for each angle, $\theta_{\rm i}$, of the half-wave plate. From Patat & Romaniello (2006) we then use the following expressions

$$F_{\rm i} = \frac{(f_{\rm o,i} - f_{\rm e,i})}{(f_{\rm o,i} + f_{\rm e,i})} \tag{1}$$

$$q = \frac{2}{N}\sum_{i=0}^{N-1} F_{\rm i}\cos\left(\frac{i\pi}{2}\right) \tag{2}$$

$$u = \frac{2}{N}\sum_{i=0}^{N-1} F_{\rm i}\sin\left(\frac{i\pi}{2}\right) \tag{3}$$

where N is the number of rotation angles of the half-wave plate. Note that for EFOSC2 we used the (arbitrary) convention that the upper image strip is the *o* beam and the lower the *e* beam. For SofI, mounted at the opposite Nasmyth port, we use the opposite convention. We then calibrate and remove the instrumental polarization from the raw measured q, u values to obtain the true observed val-

[11] https://www.eso.org/sci/facilities/lasilla/instruments/sofi/tools/sofi_scripts.html
[12] Located in Oadby, Leicester, UK.
[13] planewave.com

ues using a Mueller matrix fit to all standard star observations (see Section 3.2).

As discussed in Section 2.3.2, SofI requires rotation of the Wollaston prism with respect to the detector to take the equivalent polarimetric measurements. To convert the measured Stokes parameters into linear polarization degree (P) and angle of polarization (θ), we used the following relations

$$P = \sqrt{q^2 + u^2} \tag{4}$$

$$\theta = \frac{1}{2}\arctan\left(\frac{q}{u}\right) + \phi \tag{5}$$

$$\phi = \begin{cases} 0^\circ, & \text{if } q > 0 \text{ and } u \geq 0 \\ 180^\circ, & \text{if } q > 0 \text{ and } u < 0 \\ 90^\circ, & \text{if } q < 0 \end{cases} \tag{6}$$

where equation (6) is for an offset angle, ϕ, dependent on the signs of q and u. This aligns the polarization angle to the common definitions of position angle (where the $+Q$ vector is North, Wiersema et al. 2012b; de Serego Alighieri 2017). The errors on q and u were calculated following the method described in Patat & Romaniello (2006) and the errors on P and θ were calculated through the propagation of the q and u errors.

The instrumentally corrected polarization of an optical source does not reflect the true polarization value due to polarization bias (Serkowski 1958). This effect is a function of $P/\sigma_{\rm P}$. There are a number of estimators that can correct for polarization bias such as the Maximum Likelihood estimator (Simmons & Stewart 1985) and Wardle–Kronberg estimator (Wardle & Kronberg 1974). We use the modified asymptotic (MAS) estimator defined in Plaszczynski et al. (2014) by the following expression

$$P_{\rm MAS} = P - \sigma^2 \left[\frac{1 - {\rm e}^{\frac{-P^2}{\sigma_P^2}}}{2P}\right] \tag{7}$$

where $P_{\rm MAS}$ is the modified asymptotic estimation of the true polarization P_0 and σ_P represents the standard error on the polarization measurement.

In most cases where the signal-to-noise ratio (S\N) is high the distribution of P can be taken to be approximately Gaussian . As the S/N of a source decreases the distribution of P begins to follow a Rice distribution (Rice 1944). This occurs when $\eta < 2$ where $\eta = P$(S/N) and leads to non-symmetric and complex confidence interval calculations. For the majority of our observations, where $P_{\rm MAS}/\sigma_{\rm P} \gtrsim 3$, the S/N is sufficiently high to quote $P_{\rm MAS} \pm \sigma_{\rm P}$ for our results. Our quoted errors are close to the real 68 per cent confidence intervals but we probably underestimate the true error by a small amount (Simmons & Stewart 1985; Sajina et al. 2011).

For cases where the S/N is low (which we take as $P_{\rm MAS}/\sigma_{\rm P} < 3$), we quote a 95 per cent upper limit on the degree of true polarization given by

$$P^{\alpha}_{\rm Upper} = P_{\rm MAS} + P_\alpha(1 - \beta {\rm e}^{-\gamma P_{\rm MAS}}) \tag{8}$$

where $\alpha = 0.95$, $P_\alpha = 1.95\sigma_{\rm P}$, $\beta = 0.22$, and $\gamma = 2.54$ in the case of a 2σ upper limit (Plaszczynski et al. 2014). Given the relatively small number of sources in our survey (< 100) a full statistical treatment of the distribution of formal measurements (e.g. Quinn 2012) would not result in changes to our conclusions.

3.2 Calibrating instrumental polarization

As discussed in Section 2.2 we require an accurate instrumental calibration to ensure that our values are not dominated by instrumental polarization systematics and our results are meaningful. We aim for calibration accuracy $P_{\rm sys} \lesssim 0.2$ per cent. At the time of observing there were no comprehensive investigations of SofI and EFOSC2 instrumental polarization behaviour in the literature. Both EFOSC2 and SofI are Nasmyth mounted and should therefore exhibit high levels of polarization, with a strong dependency on PA and wavelength.

In the EFOSC2 run we observed a sample of five unpolarized and three polarized standard stars over our three observing nights in the V, B, and R bands for a sum total of 48 and 21 datapoints, respectively. In the SofI run we observed five unpolarized and one polarized standard star in the Z band for a sum total of 14 and 2 datapoints, respectively. Observation times were chosen to sample the PA dependence well. EFOSC2 is a focal reducer instrument, with somewhat similar optics to the Focal Reducer and low dispersion Spectrograph (FORS) instruments on the Very Large Telescope (VLT). The FORS instruments show pronounced off-axis instrumental polarization but low values on-axis (Patat & Romaniello 2006). We therefore positioned each source, science and calibration object in the centre of the CCD, near the optical axis, as part of the acquisition procedure. As such, our calibration efforts do not address off-axis instrumental polarization patterns.

Our EFOSC2 calibration efforts are discussed in detail in a separate publication (Wiersema et al. 2018). We will summarize the main points below, as we use an identical approach for SofI (which is not discussed in Wiersema et al. 2018).

The SofI and EFOSC2 standard star observations are reduced and analysed in the same way as the science observations. The measured q, u values for the standards are then used for the instrument modelling. As described in Wiersema et al. (2018), we prefer a Mueller matrix approach to the instrument modelling. We use a sequence of Mueller matrices following the method described in Giro et al. (2003) and Covino et al. (2014). The train of matrices is constructed to describe all key polarizing components of the instrument and telescope. We then fit for two unknown quantities in the resultant matrix (i.e. the wavelength-dependent complex index of refraction $n_{\rm c} = n - i{*}k$ where n is the refractive index and k the extinction coefficient and any angular offset between the detector and the celestial reference frame) onto the full data set described above. For both SofI and EFOSC2 the primary cause of instrumental polarization is found to be the tertiary mirror (M3) that feeds the light to the instrument. We use the prescription by Stenflo (1994) to evaluate the matrix components of M3 and the material constants (n, k) from Rakic et al. (1998) at the central wavelengths of the B,V,R filters for EFOSC2, and Z for SofI. As demonstrated in Wiersema et al. (2018), the resultant model fits the EFOSC2 q, u values of the unpolarized and polarized standards very well, resulting in calibration accuracy to levels of $P_{\rm sys} \sim 0.1$ per cent. The polarization model is expected to be dependent on time, as mirror coatings age. For SofI we follow the exact same strategy as for EFOSC2 with the only difference being the definition of o and e beams.

The matrix model follows the relation

$$[S'] = [M_{\rm T}] \times [S] \tag{9}$$

where $[S]$ is the Stokes vector representing the intrinsic polarization parameters of the source, $[M_{\rm T}]$ is the Mueller matrix representing the physical properties of the telescope (discussed above) and $[S']$ is

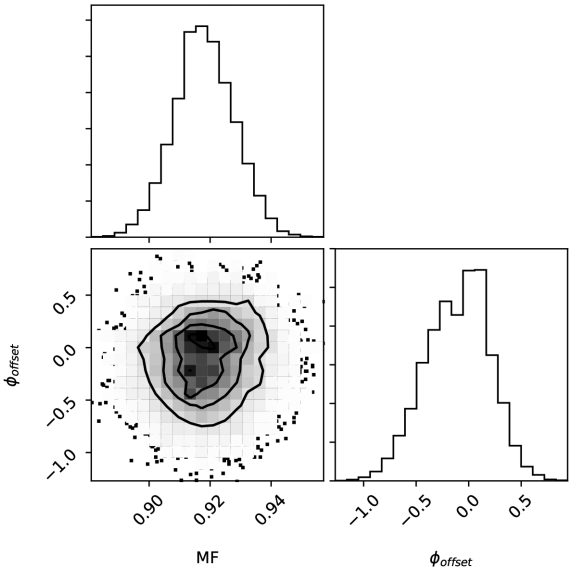

Figure 4. 2D projection of the probability distributions of the two fitting parameters for SofI calibration – the multiplication factor (MF) and the detector offset angle $\phi_{\rm offset}$.

Table 1. Detector angle offset and multiplication factor values derived from the MCMC analysis. Confidence intervals are 1σ.

$\phi_{\rm offset}$ (°)	Multiplication factor
-0.17 ± 0.3	0.92 ± 0.01

the Stokes vector representing the measured polarization parameters (a combination of real and instrumental polarization). To extract the true (instrumental polarization corrected) Stokes vector we can simply use the inverse matrix:

$$[S] = [M_{\rm T}]^{-1} \times [S'] \tag{10}$$

The matrix element values depend on PA so to correct the measured q, u from Section 3 we evaluate the matrix elements above using the PA at the middle of the polarimetric observation set. As our exposure times are relatively short, the uncertainty in PA is small.

Fig. 4 shows the projection of the probability distributions of the two fitting parameters, derived using a Markov Chain Monte Carlo (MCMC) code (EMCEE; Foreman-Mackey et al. 2013). As observed with the EFOSC2 calibration (Wiersema et al. 2018), we find the parameter space is non-degenerate with both parameters following a normal distribution. The median values (peaks) of the probability distributions and 1σ confidence intervals can be seen in Table 1.

We show the SofI calibration model using the above fitting parameter values in Fig. 5. We compare the models to the observed unpolarized standard star Stokes parameters q, u. The measured q, u values from our observations of the unpolarized standard stars can be seen in the online-only appendix. We also observed the polarized standard star BD-12°5133 and compared the observed q, u values to the derived values from our model fitting. To achieve this we had to estimate the intrinsic Z-band polarization for BD-12°5133 using the empirical formula for the Serkowski parameters (Serkowski et al. 1975) defined by the following relation:

$$P_\lambda = P_{\lambda_{\rm max}} {\rm e}^{-{\rm K}\ln^2(\frac{\lambda_{\rm max}}{\lambda})} \tag{11}$$

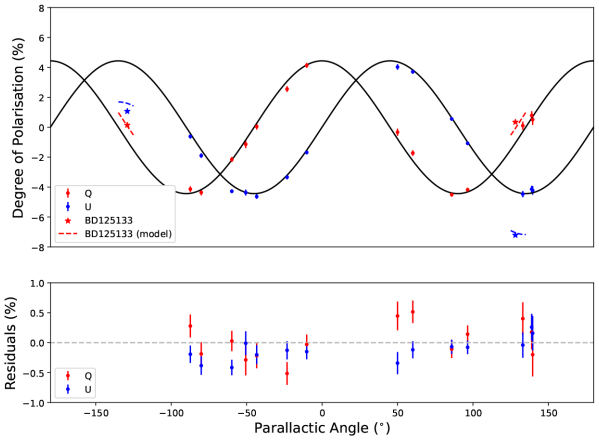

Figure 5. The top panel shows the best-fitting model for SofI instrumental polarization derived using the Mueller matrix method (black line) and measured q, u values of the unpolarized standard stars (circles) in Z-band. We have also shown the measured q and u values for the polarized star BD-12°5133 and the model which reproduces the measurements well. The bottom panel shows the residuals for the q, u, where the average residuals for the q and u fits are ∼0.12 per cent and ∼0.10 per cent, respectively.

where P_λ is the linear polarization at a given wavelength, $P_{\lambda_{\rm max}}$ is the peak linear polarization of a source and K is the width constant. Using values derived for BD-12°5133 in Cikota et al. (2017) of $P_{\lambda_{\rm max}} = 4.37(\pm0.01)$ per cent, $\lambda_{\rm max} = 505(\pm 3.5)$ nm and ${\rm K} = 1.20(\pm 0.04)$, we find an intrinsic polarization of $P = 2.93(\pm0.07)$ per cent. From the measurements of the polarization angle (∼145°) we calculate Stokes parameters of $q = 1.00(\pm0.02)$ per cent and $u = -2.75(\pm0.06)$ per cent, respectively. A good fit is found for both the unpolarized and polarized standard stars, with a calibration accuracy of $P_{\rm sys} \sim 0.2$ per cent.

There are three key points to note when comparing our SofI calibration to the EFOSC2 calibration. First, we find that the SofI calibration is not as accurate as our EFOSC2 calibration (we observed fewer standard stars during the second observing run) but is still to a level required to successfully analyse our science results. Secondly, the amplitude of the instrumental q, u as a function of PA is larger for SofI than it is for EFOSC2 (see fig. 2 in Wiersema et al. 2018). This agrees with our previous calibration of EFOSC2 in the B, V, and R bands where a larger instrumental polarization is observed at longer wavelengths. Thirdly, we derive a detector offset angle consistent with 0°. This arises from our definition of the o and e beams discussed in Section 3.1. The prescription we use for the beams is for both the SofI data analysis and calibration – the reverse of EFOSC2 and this allow us to derive this conveniently low offset. Reversing the prescription to match the beam convention used for the EFOSC2 data simply changes the derived offset angle by −90°. Providing the o and e beam ordering is kept consistent for both the calibration and data analysis, the calculated degree of polarization and polarization angle will be same for either prescription.

3.3 Polarization results

The Stokes q and u parameters (after correction for instrumental polarization, Section 3.2) of all observed sources can be seen in Table 2 along with the bias-corrected degree of polarization, P and polarization angle. We show the full range of Stokes q and u parameters for the source observations in all four filters (Fig. 6).

Table 2. Table containing the observational time and polarization properties of our chosen sources. The median observation date and PA values recorded are taken from the start of the third half-wave plate exposures. All errors are quoted to 68 per cent confidence apart from upper limits, which are quoted at 95 per cent confidence (see Section 3.1).

Source name	Filter	Obs. date (mid, MJD)	Exposure time [a] (s)	Parallactic angle (mid, deg)	q ($\times$100 per cent)	u ($\times$100 per cent)	P ($\times$100 per cent)	θ (deg)	Time Elapsed [b] (days)	Type [c]
3C 454.3	*V*	57560.4243	60	169.9	−3.88(±0.06)	11.03(±0.05)	11.70(±0.05)	54.7(±0.12)	7.21	Blazar
	V	57562.3199	2 × 60	−149.7	13.15(±0.14)	9.85(±0.15)	16.43(±0.14)	18.43(±0.24)	9.11	
	B	57562.3289	2 × 60	−152.7	14.45(±0.05)	9.98(±0.22)	17.56(±0.14)	17.32(±0.21)	9.12	
	R	57562.3380	2 × 60	−156.0	10.87(±0.38)	7.66(±0.26)	13.29(±0.34)	17.59(±0.74)	9.13	
ASASSN-16fp	*V*	57560.2842	1 × 15 + 2 × 30	−149.4	0.03(±0.02)	0.02(±0.03)	≤ 0.08	–	24.63	SN Ib
	B	57560.2920	2 × 30	−152.0	0.12(±0.14)	0.32(±0.01)	0.34(±0.05)	35.17(±4.21)	24.64	
	R	57560.2986	2 × 30	−154.2	0.07(±0.03)	0.05(±0.03)	≤ 0.10	–	24.65	
ASASSN-16fq	*V*	57559.9968	180	148.3	1.03(±0.20)	−1.01(±0.15)	1.44(±0.18)	157.89(±3.54)	23.44	SN IIP
	B	57560.0069	180	145.0	1.24(±0.54)	−1.92(±0.42)	2.24(±0.46)	151.45(±5.77)	23.45	
	R	57560.0170	180	142.0	0.67(±0.14)	−0.82(±0.11)	1.05(±0.12)	154.77(±3.29)	23.46	
ASASSN-16fs	*V*	57560.0830	2 × 180	170.9	−0.54(±0.10)	0.06(±0.11)	0.53(±0.10)	86.75(±5.28)	16.40	SN Ia
ASASSN-16ft	*V*	57559.3699	300	−139.8	−0.40(±0.36)	1.17(±0.27)	1.21(±0.28)	54.43(±6.42)	14.50	SN II
ASASSN-16fv	*V*	57559.1257	180	−42.8	0.35(±0.08)	0.05(±0.06)	0.35(±0.08)	3.86(±6.41)	12.52	SN Ia
	B	57559.1344	120	−39.1	0.01(±0.12)	0.06(±0.09)	≤ 0.22	–	12.53	
	R	57559.1418	120	−35.9	0.57(±0.09)	0.15(±0.07)	0.58(±0.09)	7.28(±4.16)	12.54	
ASASSN-16fx	*V*	57559.4174	180	−77.3	−0.20(±0.25)	−0.12(±0.18)	≤ 0.56	–	11.71	SN Ia
ASASSN-16ga	*V*	57559.2052	240	86.6	0.72(±1.32)	1.40(±1.02)	≤ 3.35	–	10.90	CV[d]
ASASSN-16gg	*V*	57559.2325	90	95.0	−1.31(±4.33)	1.01(±3.41)	≤ 8.55	–	2.24	CV[d]
	B	57559.2384	90	96.4	−6.68(±6.86)	−2.36(±5.52)	≤ 18.04	–	2.25	
	R	57559.2437	60	97.6	3.04(±3.80)	2.00(±3.05)	≤ 9.50	–	2.26	
	V	57560.2215	240	93.0	1.38(±2.95)	−6.37(±2.38)	≤ 10.77	–	3.24	
	B	57560.2408	240	97.6	−8.30(±4.42)	−2.05(±3.46)	≤ 15.98	–	3.25	
	R	57560.2537	240	100.5	7.58(±2.80)	1.19(±2.00)	≤ 12.60	–	3.26	
ASASSN-17gs	*Z*	57974.0350	5 × 3 ×60	138.5	7.87(±0.54)	−4.44(±0.43)	9.03(±0.52)	165.28(±1.63)	75.64	BL Lac
ASASSN-17km	*Z*	57973.1994	5 × 3 ×15	−96.8	0.07(±0.31)	−0.14(±0.25)	≤ 0.51	–	2.77	CV[d]
	Z	57973.4205	5 × 3 ×30	84.6	0.12(±0.35)	−0.57(±0.55)	≤ 1.39	–	2.99	
AT2016bvg	*V*	57559.1846	240	121.9	−2.21(±0.93)	−0.62(±0.83)	≤ 3.91	–	55.40	Unknown
	V	57560.1359	2 × 240	133.8	−1.57(±0.31)	0.80(±0.17)	1.73(±0.28)	76.58(±4.60)	56.35	
AT2016cvk	*V*	57559.2812	2 × 240	−80.0	−0.15(±0.60)	0.36(±0.80)	≤ 1.90	–	6.65	SN IIn
ATLAS16bcm	*V*	57560.1118	240	165.0	−0.56(±0.21)	0.06(±0.16)	≤ 0.91	–	11.64	SN Ia
ATLAS16bdg	*V*	57559.0906	180	122.8	2.12(±0.22)	0.25(±0.17)	2.12(±0.22)	3.33(±2.96)	5.60	SN Ia
	B	57559.1007	180	121.4	3.42(±0.60)	1.12(±0.48)	3.55(±0.59)	9.06(±4.72)	5.61	
	R	57559.1108	180	120.2	0.88(±0.20)	0.43(±0.15)	0.97(±0.19)	12.96(±5.49)	5.62	
ATLAS17jfk	*Z*	57974.2359	5 × 3 ×60	119.9	2.21(±0.58)	−0.85(±0.46)	2.30(±0.57)	169.47(±6.88)	6.04	Novae
CTA 102	*V*	57559.4053	60	172.3	22.46(±0.14)	1.98(±0.11)	22.53(±0.14)	2.48(±0.17)	10.97	Quasar
	Z	57973.3216	5 × 3 ×60	151.4	5.70(±0.47)	3.32(±0.40)	6.58(±0.45)	15.13(±1.97)	31.81	
Gaia16aau	*V*	57559.3508	240	−60.0	−0.14(±0.06)	−0.17(±0.05)	0.22(±0.05)	115.70(±7.03)	146.58	RCB Star
Gaia16agw	*V*	57559.1566	240	101.6	−0.01(±0.31)	0.05(±0.20)	≤ 0.36	–	111.86	Blazar[d]
Gaia16alw	*V*	57562.2083	3 × 300	148.7	−5.45(±1.23)	−1.33(±0.29)	5.48(±1.20)	96.84(±6.13)	64.98	Unknown
Gaia16aoa	*V*	57562.0209	3 × 240	111.0	0.43(±0.61)	−1.58(±0.36)	1.59(±0.38)	142.59(±6.65)	44.27	Unknown
Gaia16aob	*V*	57560.0454	240	99.0	−0.10(±0.17)	0.38(±0.13)	0.37(±0.12)	52.10(±9.53)	41.30	AGN[d]
Gaia16aok	*V*	57559.0372	2 × 300	92.8	11.51(±0.07)	0.22(±0.31)	11.51(±0.07)	0.56(±0.18)	38.79	Unknown
Gaia16aol	*V*	57560.0651	120	120.7	−0.45(±1.54)	−1.99(±1.21)	≤ 4.08	–	40.05	SN[d]
Gaia16aoo	*V*	57559.0088	240	137.1	0.58(±1.06)	0.23(±0.89)	≤ 2.21	–	37.74	SN IIP
Gaia16aqe	*V*	57562.4013	3 × 180	−123.5	1.12(±0.59)	−0.23(±1.41)	≤ 2.07	–	31.68	SN Ia
Gaia17blw	*Z*	57974.3484	5 × 3 ×60	−70.2	0.57(±0.72)	0.14(±0.55)	≤ 1.65	–	65.32	SN IIn
Gaia17bro	*Z*	57974.3966	5 × 3 ×60	−73.8	−0.81(±0.74)	−0.33(±0.57)	≤ 1.99	–	37.85	SN IIn
Gaia17bvo	*Z*	57974.0793	5 × 2 ×60	64.1	−1.03(±0.32)	8.32(±0.25)	8.37(±0.25)	48.53(±0.86)	16.76	YSO[d]

Table 2 – *continued*

Source name	Filter	Obs. date (mid, MJD)	Exposure time [a] (s)	Parallactic angle (mid, deg)	q (×100 per cent)	u (×100 per cent)	P (×100 per cent)	θ (deg)	Time Elapsed [b] (days)	Type [c]
Gaia17bwu	*Z*	57973.1470	5 × 3 ×60	84.1	0.92(±0.33)	0.76(±0.27)	1.16(±0.30)	19.81(±7.25)	12.08	Red Star
Gaia17bxl	*Z*	57973.2327	5 × 3 ×60	− 82.3	5.22(±3.13)	− 0.34(± 2.20)	≤ 10.45	–	9.39	SN
Gaia17byh	*Z*	57973.0822	5 × 3 ×60	− 21.5	− 0.29(± 1.29)	− 0.16(± 0.97)	≤ 2.22	–	7.45	SN Ic
Gaia17byk	*Z*	57974.1218	5 × 3 ×60	90.7	2.98(±0.59)	− 5.21(± 0.46)	5.99(±0.49)	149.88(±2.35)	7.54	Unknown
Gaia17bzc	*Z*	57974.1937	5 × 2 ×60	98.0	4.20(±0.74)	5.46(±0.57)	6.86(±0.64)	26.21(±2.65)	5.86	Unknown
GX 304-1	*V*	57562.0537	5	37.9	− 6.75(± 0.16)	− 0.86(± 0.12)	6.80(±0.16)	93.58(±0.67)	35.01	HMXB
	B	57562.0557	5	37.9	− 5.98(± 0.45)	− 1.55(± 0.35)	6.17(±0.45)	97.29(±2.07)	35.01	
	R	57562.0578	5	37.9	− 6.77(0.08)	− 0.75(± 0.06)	6.80(±0.08)	93.08(±0.34)	35.01	
MASTER OT J023819	*Z*	57974.2921	5 × 2 ×60	− 75.4	0.20(±0.25)	− 0.66(± 0.20)	0.66(±0.20)	143.25(±8.36)	0.34	AGN[d]
MASTER OT J220727	*V*	57559.3162	2 × 240	− 143.9	0.20(±0.31)	− 1.09(± 0.34)	1.06(±0.34)	140.24(±8.76)	3.48	SN Ia
OGLE16aaa	*V*	57560.3271	3 × 240	− 76.6	1.79(±0.43)	− 0.49(± 0.31)	1.81(±0.42)	172.33(±6.44)	150.82	TDE
P13 NGC7793	*V*	57560.3716	3 × 240	− 88.8	3.01(±1.80)	− 2.06(± 1.62)	≤ 6.54	–	31.92	ULX
PG 1553+113	*V*	57560.2030	30	142.7	2.34(±0.10)	4.59(±0.08)	5.15(±0.09)	31.50(±0.49)	54.42	BL Lac
	B	57560.2062	30	141.8	2.38(±0.16)	4.69(±0.13)	5.26(±0.13)	31.55(±0.73)	54.42	
	R	57560.2094	30	140.8	2.30(±0.08)	4.19(±0.07)	4.78(±0.07)	30.62(±0.43)	54.43	
PKS 1510-089	*V*	57558.9952	45	− 128.1	5.81(±0.18)	− 6.56(± 0.15)	8.76(±0.16)	155.77(±0.54)	19.45	Blazar
	V	57560.1548	45	132.8	0.39(±0.21)	− 3.12(± 0.16)	3.14(±0.16)	138.55(±1.49)	20.61	
	V	57562.1839	60	124.4	0.48(±0.60)	− 1.92(± 0.33)	1.94(±0.35)	142.03(±5.08)	22.64	
PKS 2023-07	*V*	57559.2568	240	− 147.2	7.35(±0.36)	− 0.55(± 0.28)	7.36(±0.35)	177.84(±1.38)	64.83	Blazar
PS16cnz	*V*	57559.0751	240	160.3	− 0.29(± 0.18)	− 0.19(± 0.13)	≤ 0.60	–	26.16	Unknown
PS16crs	*V*	57562.1494	2 × 300	158.6	− 0.99(± 0.13)	1.11(±1.36)	≤ 3.72	–	22.68	SN Ia
PS16ctq	*V*	57560.1844	2 × 240	102.4	− 0.20(± 0.23)	− 0.04(± 0.44)	≤ 0.50	–	9.16	Unknown
PS16cvc	*V*	57560.4040	240	150.0	0.40(±0.18)	0.15(±0.14)	≤ 0.71	–	1.90	SN Ia
	V	57562.3638	3 × 180	163.7	0.03(±0.07)	0.39(±0.18)	≤ 0.74	–	3.86	
SXP 15.3	*Z*	57973.2826	5 × 3 ×30	− 31.2	0.43(±0.42)	− 0.72(± 0.33)	≤ 1.45	–	12.07	XRB
XTE J1709-267	*V*	57562.0869	3 × 240	− 102.6	− 0.34(± 0.11)	1.21(±0.44)	≤ 2.00	–	20.71	LMXB

[a] Exposure times are given per angle. In the case of the SofI *Z* band data, the exposure time is shown as NEXP × NDIT × DIT, where DIT is the detector integration time in seconds, NDIT the number of DIT integrations that is averaged to make a single output file, and NEXP the number of separate NDIT × DIT files. In the case of EFOSC2, the exposure time is shown as NSET × EXPT, where EXPT is the integration time per angle, and NSET is the number of consecutive four-angle cycles within the observation.
[b] The reader is reminded that time elapsed refers to the time between the distribution of the alert and our polarimetric observations.
[c] For additional information about the classification of the tabulated sources see the online appendix.
[d] Classification not spectroscopically confirmed.

This is further split into the *V* band observations of each transient type (Fig. 7) and each SNe class (Fig. 8).

Fig. 9 displays the polarimetric parameter space covered by SPLOT – analogous to the second panel of Fig. 1. The figure shows the bias-corrected polarization against time elapsed. The time elapsed is calculated from the time the source alert was distributed to the mid-point time when we took our observations (column three in Table 2). In the case of most new transients, the alert corresponds to the discovery of the source. For sources with historic observations we use the date of a recent alert of increased activity, where the time elapsed is calculated from time of the recent outburst alert to the time we took our observations.

For additional information on each individual source see the online-only appendix. We also provide light curves where possible to highlight where our observations lie with respect to the evolution of the source (e.g. are we observing before or after light-curve peak for SNe and novae).

4 SOURCE PHOTOMETRY

Each target in the first observing run (EFOSC2) was imaged in the *V* band, directly following the polarimetric sequence. In the second observing run (SofI), the same method was followed in the *Z* band. A small subset were also observed in the *V* and/or *B* bands using the UL50 at Oadby as part of an ongoing transient programme. Photometry was performed in the same manner for all observations.

Due to the weather conditions at both La Silla and in Oadby, our observing nights were not photometric and field stars were used for calibration, wherever possible. We cross-match field stars within the telescopes respective FOV with the AAVSO Photometric All-Sky Survey (APASS), the Sloan Digital Sky Survey-DR13 (SDSS), the PanSTARRs DR1 (Chambers et al. 2016) and the Skymapper Southern Sky Survey (Keller et al. 2007) catalogues for the *V* and *B* band images. SDSS, Pan-STARRS, and Skymapper do not have direct photometric observations in the *V* and *B* bands, so both the

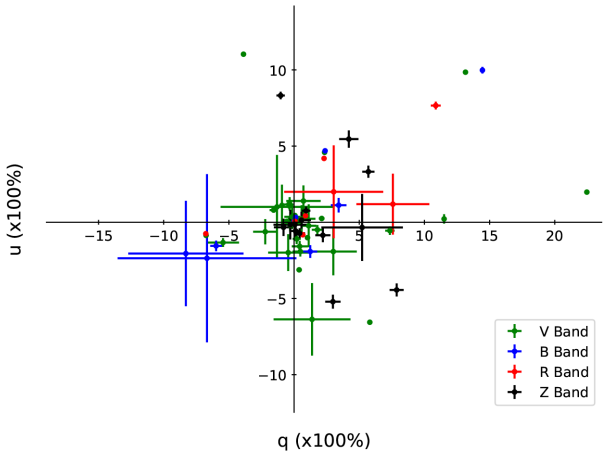

Figure 6. Stokes q and u parameters in the V, B, R, and Z bands for all SPLOT sources. The plot shows that the SPLOT survey observed sources covering a large area of q, u parameter space.

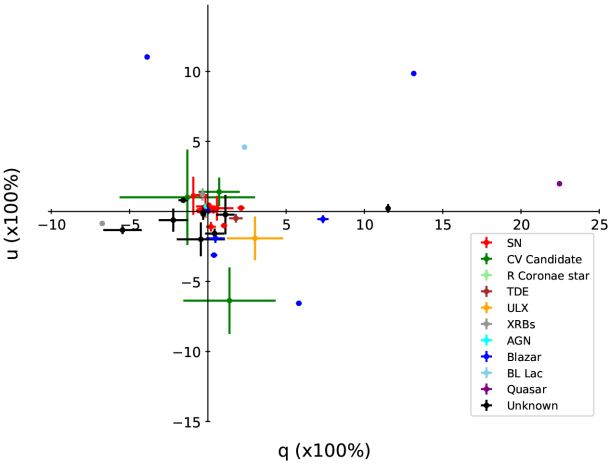

Figure 7. Stokes q and u parameters (V- band only) categorized by source type. We aimed to observe both a variety of transient sources with SPLOT and cover a large area of parameter space.

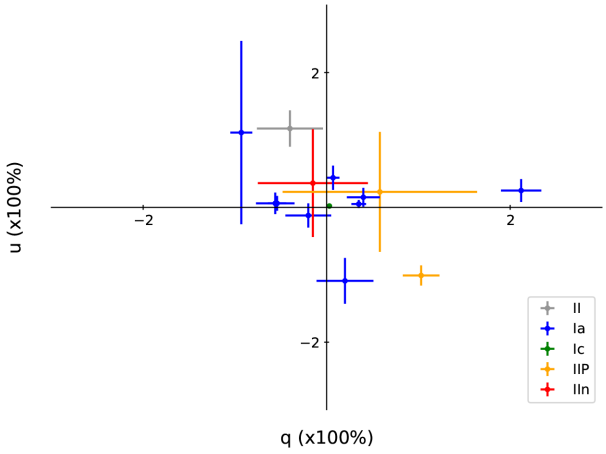

Figure 8. Stokes q and u parameters (V- band only) separated into SN types. The q and u measurements shown are not corrected for line-of-sight dust. The figure highlights the significance of line-of-sight dust induced polarization especially for type Ia SNe where we expect intrinsic $P \lesssim 0.3$ per cent.

V and B magnitudes and associated errors were calculated from the following expressions

$$M_{\rm V} = M_{\rm g} - 0.5784(M_{\rm g} - M_{\rm r}) - 0.0038 \quad (12)$$

$$M_{\rm B} = M_{\rm g} + 0.3130(M_{\rm g} - M_{\rm r}) + 0.2271 \quad (13)$$

$$\sigma_{{\rm M}_V} = \sqrt{(0.4216\sigma_{{\rm M}_g})^2 + (0.5784\sigma_{{\rm M}_r})^2} \quad (14)$$

$$\sigma_{{\rm M}_B} = \sqrt{(1.3130\sigma_{{\rm M}_g})^2 + (0.3130\sigma_{{\rm M}_r})^2} \quad (15)$$

where $M_{\rm g}$ and $M_{\rm r}$ are the catalogue field star magnitudes in the SDSS r and g bands and $M_{\rm V}$ and $M_{\rm B}$ are the calculated equivalent star magnitudes in the V and B bands (the expressions are taken from the SDSS transformations page under Lupton 2005[14]). Additionally, $\sigma_{{\rm M}_g}$ and $\sigma_{{\rm M}_r}$ are the 1σ errors in the g and r bands with $\sigma_{{\rm M}_V}$ and $\sigma_{{\rm M}_B}$ the derived errors for the V and B bands.

Source Extractor (SExtractor; Bertin & Arnouts 1996) was used to calculate the magnitudes of all sources using apertures matched to the seeing FWHM. The SExtractor catalogue output was then cross-matched with the catalogues listed above. Any APASS, SDSS or Pan-STARRS objects that were coincident with a detected source to within ≤ 1 arcsec were matched up. Objects that we suspected were not stars but other astrophysical objects (i.e. galaxies) were filtered out. The relation between the SExtractor instrumental magnitudes and catalogue magnitudes was fit with a first degree polynomial to calculate zero-points (we ignore colour terms and atmospheric extinction); outliers that were $> 3\sigma$ away from the best-fitting line were clipped during the fitting process.

We note that although the SDSS, Pan-STARRs and Skymapper r and g filters are very similar, they are not identical in properties. The effect on measured magnitudes is small but not negligible when we apply the filter transformations described above; there is a small uncertainty associated with this effect. The SDSS filter transformations were calculated using measurements from a large sample of stars. Therefore, there is a small additional uncertainty on the resulting magnitudes (typically 0.01 mag). In light of these issues, the errors on our calculated magnitudes may be underestimated by up to ~ 0.1 mag.

We incorporated a similar method for the sources for the Z band images during the second observing run. All sources were at low declinations due to high wind observing constraints, with a large number residing at declination $< -30^\circ$ and therefore most targets only appeared in the Skymapper catalogue. The SofI Z filter is not identical to either the SDSS, Pan-STARRS or Skymapper z filters and transformations between the bands is not well known. We therefore only provide a rough estimate for the magnitudes.

Some SPLOT target fields had very few field stars that could be used: the EFOSC2 and SofI FOVs are 4.1 × 4.1 and 4.9 × 4.9 arcmin, respectively. These cases could not be calibrated using this method. As the weather on our observing run was highly variable we could not accurately interpolate between images to estimate the magnitude zero points, and so we do not calculate a magnitude for these sources. See Table 3 for full set of results.

[14] http://www.sdss3.org/dr8/algorithms/sdssUBVRITransform.php

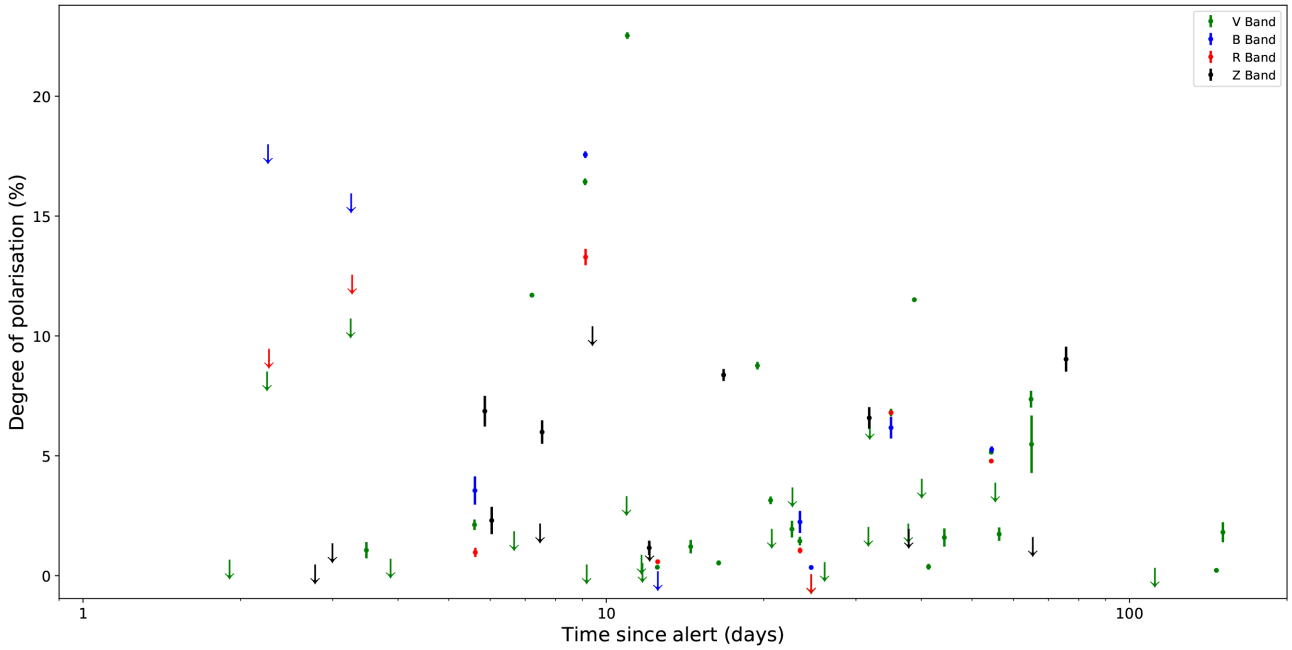

Figure 9. Polarization against time elapsed between the distributed alert. Polarization value errors are quoted to 68 per cent confidence and all limits are quoted to 95 per cent confidence. See Table 2 for individual source details.

5 DISCUSSION: SURVEY RESULTS

The SPLOT survey was conducted as a pilot investigation to determine the feasibility of an optical polarimetric survey of transient astrophysical sources. To do this we set ourselves a number of goals for SPLOT, outlined in Introduction. Below, we discuss how well the results of SPLOT fit in our initial aims.

5.1 Transient selection and sample breadth

Our first and arguably most important goal was to observe a fairly large number of sources during our observing runs. This was important for a number of reasons: we wanted to sufficiently sample a host of different transient phenomena, sample a representative fraction of the contents of real-time alert streams produced by current facilities and cover a large volume of the multidimensional parameter space of properties where transient events exist.

To maximize the number of sources we could observe, and reduce the uncertainties on the calibration, we aimed for short exposure times – with the longest observation blocks requiring execution times of no more than one hour. Our shortest execution times were ∼15 min where we were limited by the overheads (i.e. source acquisition, read-out times). As discussed in detail in Section 2.2, we had variable weather conditions throughout our two observing runs. We lost over two and a half nights out of a scheduled eight to bad weather with the addition of the *Gaia* alert system becoming unavailable for the duration of our first observing run. For weather conditions where the seeing FWHM was above ∼1.5 arcsec we struggled to observe the very faintest sources whilst also keeping our exposures relatively short. These limitations restricted the total parameter space we could fully explore – experience from the Palomar Transient Facility has shown that studying transients found at magnitudes $\gtrsim$ 20 mag greatly expands this transient parameter space yield. As seen from Table 2, we observed 48 optical transients excluding calibration sources utilizing a whole host of transient survey streams. If we further break down our sample into classifications, we observed the following:

(i) 19 SNe/SNe candidates
(ii) 8 sources with no follow-up classification observations
(iii) 9 AGNs (including BL Lacs, Blazars, strong candidate variables, etc.)
(iv) 3 XRBs
(v) 3 cataclysmic variable candidates
(vi) 1 ultraluminous X-ray source
(vii) 1 tidal disruption event
(viii) 1 extragalactic Novae
(ix) 1 R Coronae Borealis star
(x) 1 young stellar object
(xi) 1 brightening red star

The above list shows that we observed a fairly diverse range of transient sources and by design a large number of sources with no prior classification. Additionally, we covered a reasonable volume of the multidimensional parameter space partially described by the two windows in Fig. 1. Our sample representation of the polarimetric–time domain (Fig. 9) highlights the depth of the survey. Our photometry further supports this – we covered sources whose apparent magnitudes lay between 14 and 20 mag. However, the variable weather limited how faint we could observe during times of poor conditions. Fig. 10 represents a visualization of the explored parameter space of the SPLOT survey.

5.2 Galactic dust induced polarization

The polarization measurements we made have not been corrected for line-of-sight dust and therefore contain the effects of dust scattering from both the Milky Way and host. The magnitude of this effect cannot be diagnosed directly from SPLOT *V* data alone. Some effects of dust can be seen in our sample results of extragalactic sources, such as the small number of type Ia SNe that

Table 3. Table containing the calculated brightness of each source and the observation date for images where a magnitude could be obtained. All errors on the magnitudes are quoted to 1σ. Approximate magnitudes are given for SofI photometry (see Section 4).

Source name	Filter	Exposure time (s)	Obs. date (mid, MJD)	Magnitude (AB)
3C 454.3	*V*	30	57560.4269	14.26(±0.02)
	V	30	57605.0446	15.11(±0.01)
	V	30	57645.0503	15.99(±0.03)
	B	30	57663.9217	16.50(±0.04)
	B	30	57696.8793	16.04(±0.01)
	B	30	57710.8737	16.55(±0.02)
	V	30	57721.8178	15.82(±0.10)
ASASSN-16fp	*V*	20	57560.3017	14.10(±0.02)
	V	30	57605.0196	15.85(±0.02)
ASASSN-16fs	*V*	30	57560.0934	17.21(±0.04)
ASASSN-16ft	*V*	60	57559.3780	17.15(±0.02)
ASASSN-16fv	*V*	30	57559.1458	15.04(±0.01)
ASASSN-16fx	*V*	30	57559.4228	17.06(±0.03)
ASASSN-16ga	*V*	30	57559.2120	19.04(±0.04)
ASASSN-16gg	*V*	30	57559.2463	19.44(±0.08)
	V	60	57560.2604	19.78(±0.09)
ASASSN-17gs	*Z*	60	57974.0054	∼16.5
ASASSN-17km	*Z*	5	57973.1920	∼13.7
	Z	5	57973.4067	∼13.7
AT2016bvg	*V*	30	57559.1913	18.10(±0.07)
	V	60	57560.1491	18.26(±0.02)
AT2016cvk	*V*	60	57559.2907	17.77(±0.05)
ATLAS16bcm	*V*	60	57560.1186	17.61(±0.02)
ATLAS16bdg	*V*	30	57559.1162	16.70(±0.02)
ATLAS17jfk	*Z*	60	57974.2101	∼18.6
CTA 102	*V*	20	57559.4079	15.48(±0.02)
	V	30	57605.0320	16.58(±0.02)
	B	30	57663.9612	16.48(±0.02)
	B	30	57696.8702	15.05(±0.01)
	B	30	57710.8650	14.65(±0.02)
	V	30	57721.8110	13.12(±0.01)
	B	30	57721.8600	13.89(±0.02)
	V	30	57721.8647	13.19(±0.01)
	Z	60	57973.2963	∼15.7
	B	30	58062.8560	17.04(±0.03)
Gaia16aau	*V*	60	57559.3576	14.74(±0.18)
Gaia16agw	*V*	30	57559.1634	17.58(±0.01)
Gaia16alw	*V*	60	57562.2399	19.26(±0.06)
Gaia16aoa	*V*	60	57562.0405	19.16(±0.03)
Gaia16aob	*V*	60	57560.0522	17.27(±0.01)
Gaia16aok	*V*	60	57559.0532	19.83(±0.11)
Gaia16aoo	*V*	30	57559.0156	18.37(±0.04)
Gaia17blw	*Z*	60	57974.3190	∼17.6
Gaia17bro	*Z*	60	57974.3714	∼16.8

Table 3 – *continued*

Source name	Filter	Exposure time (s)	Obs. date (mid, MJD)	Magnitude (AB)
Gaia17bxl	*Z*	60	57973.2071	∼19.4
Gaia17byh	*Z*	60	57973.0562	∼17.3
MASTER OT J023819	*Z*	60	57974.2733	∼14.8
MASTER OT J220727	*V*	60	57559.3293	18.29(±0.02)
PG 1553+113	*V*	30	57508.0162	16.18(±0.02)
PKS 1510-089	*V*	20	57558.9975	16.02(±0.01)
	V	20	57560.1571	16.12(±0.02)
PKS 2023-07	*V*	90	57559.2635	18.13(±0.01)
PS16cnz	*V*	60	57559.0819	17.28(±0.02)
PS16ctq	*V*	60	57560.1976	18.64(±0.02)
PS16cvc	*V*	30	57560.4108	16.74(±0.01)
	V	30	57605.0560	16.55(±0.02)
SXP 15.3	*Z*	10	57973.2692	∼15.0
XTE J1709-267	*V*	90	57562.1066	17.87(±0.01)

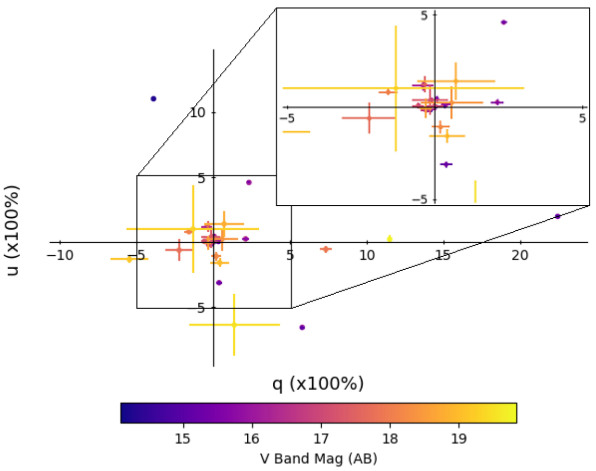

Figure 10. Stoke's *q* and *u* parameters (*V*- band only) overplotted with the accompanying AB magnitude. This plot demonstrates the photometric-polarimetric parameter space covered by SPLOT. The insert represents a zoomed-in view of the central sources in the figure (*q*, *u* values within ±5 per cent).

exhibit significant polarization measurements – suggesting a large contribution from column dust (see Fig. 8). SPLOT also contains several sources that are at low Galactic latitude and several sources that were additionally observed in the *B* and *R* bands. 3C 454.3 was observed in multiple bands and showed significant wavelength variations; a decrease in ∼4 per cent between the *B* and *R* band polarization measurements. Likewise, ASASSN-16fq, ATLAS16bdg and GX 304-1 exhibited similar behaviour but to a smaller extent. Therefore, to fully characterize wavelength-dependent behaviour, multiband snapshots would be required.

A future survey can therefore estimate the Galactic dust contribution to polarization measurements in several ways. By using field stars measurements in each set of polarimetry data, an average field star polarization value could be derived. This could be used as a proxy for the Milky Way dust contribution to polarization at those coordinates and with a high number of sources could slowly build up a Galactic map – with the *Gaia* DR2 release providing accurate astrometry and distances to a vast number of sources (Lindegren et al. 2018) this could be achieved, however, it must be noted that relatively nearby field stars do not probe the full Galactic line of sight. The FOVs of both EFOSC2 and SofI are too small to obtain a sufficient number of field stars with most sources so we were unable to attempt this during SPLOT. A value could also potentially be estimated via polarimetric sky surveys (e.g. SOUTH POL, Magalhaẽs et al. 2012) or via high-resolution reddening and distance maps of field stars to name a few methods. Dust could then become a crucial parameter in many of these surveys. Many explosive transients show interplay between local dust, gas, and photon emission. A large snapshot sample would be able to couple the retrieved polarization values to models and spectroscopic observations (e.g. Zelaya et al. 2017). Similarly, in recent years unexpected Galactic filamentary structures have been found in long-wavelength radio polarization observations, some of which have also been seen in *Planck* dust polarization maps (e.g. Zaroubi et al. 2015). Intrinsically unpolarized transients can play a useful role in tests of the dust induced polarization in transmission in these fields, as they are bright and can probe the full Galactic dust column.

5.3 The effect of practical constraints

We also highlighted our goal to investigate the impact of practical constraints on the success of a SPLOT-like survey. We discuss the effects these constraints had on our survey below.

5.3.1 Weather conditions

The varied weather conditions had a significant impact on the survey. In total we lost two and a half out of eight observing nights completely (∼31 per cent of our allocated time) restricting our total sample size. In periods of poor conditions (thick cloud, very poor seeing, wind), we favoured some bright sources and/or sources with long-lasting outburst durations. This resulted in a sample made of some sources brighter than we had initially aimed for.

During both of our runs we were in bright time, where the Moon was near full and up most of the night. This creates an additional sky background which is highly polarized and therefore affects q and u in different ways for a source near to the Moon (see Fig. 3: in the middle panel, the background is very different for the o and e image). In nights of thin cloud, prominent Moon haloes created an additional annulus zone with strongly enhanced polarized sky background, resulting in additional pointing restrictions. The Moons influence on the sample is largely limited to an increased $\sigma_{\rm P}$ for a small subset of sources and similarly it limited exposure times for a subsample.

If we had obtained eight nights of decent weather conditions – our sample size would have been closer to 80 – 100 sources and perhaps we could have sampled a larger number of sources fainter than $\sim$ 19.5 mag.

5.3.2 Instrumental calibration

As discussed in Sections 2.3 and 3.2, the Nasymth mounted EFOSC2 and SofI both induce a high level of polarization which must be corrected for to retrieve accurate science measurements. We used a Mueller matrix approach to model the physical telescopic system. The tertiary mirror (M3) that reflects the light towards the detector at a 45° angle was found to induce the vast majority of the instrumental polarization. We successfully calibrated both EFOSC2 and SofI with calibration accuracies of $P_{\rm sys} \lesssim 0.1$ per cent and 0.2 per cent, respectively. The success of this calibration not only is sufficient to achieve our initial aims but has the potential to be expanded to other similar instruments and to various other optical filters. For a full discussion on our calibration method see Wiersema et al. (2018). Future calibration pipelines could also include correcting for instrumental polarization away from the optical axis – something not covered by our efforts.

5.3.3 Extrapolating light curves

Many of the transients targeted with SPLOT had fairly large delays between discovery/alert and SPLOT observation (see Fig. 9). We had to extrapolate the discovery magnitude to the epoch of SPLOT observation. This was often uncertain, especially for sources with no additional follow-up. Fast decaying transients; e.g. some Cataclysmic Variable (CV) outbursts and some unknown transients were occasionally much fainter than expected and therefore have larger polarimetric uncertainties than the uncertainty limits we aimed to achieve (see Table 2). The periods of poor weather conditions often added to this problem meaning exposure times had to be adjusted. If, during the four angle polarimetric sequence, the weather deteriorated quickly it was harder to avoid increases in polarimetric error. We aborted observations for two sources which had faded too much to provide a reasonable polarimetric uncertainty within a reasonable execution time.

5.4 Science results precision

Our final aim was to achieve results with enough precision to deliver scientific conclusions for individual sources. We had aimed for polarimetric uncertainties of $\sigma_{\rm P} \sim 0.2$ per cent for bright sources and $\sigma_{\rm P} \sim 0.5$ per cent for the faintest sources. The calibration discussed above achieved our required target for constraining the induced instrument polarization. However, the majority of the measured uncertainties were dependent on the weather and during periods of poor weather our polarimetric uncertainties were greater than we had aimed for (see Table 2).

5.5 Overall feasibility of a SPLOT-like survey

5.5.1 SPLOT results

For SPLOT, we aimed at a sample size of ∼50 – 60 sources in V-band, with a magnitude cap described in Section 2. Though we did not achieve this number we can conclude the following about the survey. The SPLOT polarization results (see Table 2) showed a mixed success rate. For observing periods with clear weather and little cloud, the required flux sensitivity and result precision could be achieved in the short execution times we set ourselves (below ∼1 H), in particular in the EFOSC2 run. The effects of rapidly deteriorating seeing and cloud coverage resulted in some measurements failing to reach our aims. The SofI measurements have larger uncertainties than the EFOSC2 ones and the SofI sample is brighter than the EFOSC2 one due to several factors. The instrument sensitivity considerations (a typical blue or flat-spectrum transient would require longer execution time with SofI Z-band observations than with EFOSC2 V-band observations), the weather and seeing conditions and the polarimetric accuracy achievable from the calibration of SofI. Our polarimetric results do highlight that a SPLOT-like imaging polarimetry survey of transients is not more expensive than a run-of-the-mill spectroscopic transient classification program, for the snapshot single-band strategy targets.

5.5.2 Single- or multiband measurements

There is no doubt that spectropolarimetry would provide scientifically superior data sets than broad-band imaging polarimetry. This is especially true for sources that exhibit intrinsic wavelength-dependent continuum polarization, strong emission lines exhibiting polarization structure and sources with high levels of foreground dust. However, as also stated in Section 2.1, the execution time will limit such a survey to only the very brightest subsample. This would result in similar spectropolarimetry surveys being unable to sample the fainter transient events, cutting out volumes of parameter space containing transients of high interest.

To make comparisons between single and multiband measurements, observing time was set aside to observe a small fraction of SPLOT sources in B,V, and R rather than only in V. These were mainly bright sources, but were not otherwise pre-selected on source type. Bad weather meant this sample is small but some sources show wavelength-dependent polarization that is consistent with dust scattering dominating the signal. As discussed above, separating this dust components would require repeat visit observations with multiple broad bands or observations deeper into the infrared. The SofI Z-band data should show lower dust polarization effects, but the sample is smaller and we cannot make any general conclusions on the dust contributions.

5.5.3 Snapshot or multi-epoch measurements

The arguments for snapshots as opposed to multi-epoch polarimetry are similar to that of single or multiband polarimetry. In the first run with EFOSC2, half a night was set aside for repeat visits of a small subset of transients to get variability time-scales from hours to several days. The weather conditions meant that only a small subset could be done and, as such, the sample with repeat visits is small (Table 2). We see the benefit of multiple epoch observations from measurements of PKS 1510–089 where the polarization significantly decreases over a period of four days, highlighting important science such as how the internal structure of a source can vary over small time-scales. As interstellar dust polarization is not time dependent you can be confident that short-scale polarization variability between observing epochs (as discussed above) is, at least in part, intrinsic to the target source. Multi-epoch observations also have the added benefit of probing the wavelength-dependent contribution of the host galaxy dust contribution, which can be significant and vary from the Galactic Serkowski-like model. The downside to this multi-epoch type of survey is that uncovering the temporal behaviour of these sources comes at the cost of survey sample size. This trade-off between sample size and depth of follow-up must always be addressed for polarimetric surveys such as SPLOT.

Our results have shown that even short exposure, single-epoch photometry can provide scientific value for a number of sources. Future surveys may opt to run multi-epoch observations to increase the scientific value obtained per source on smaller samples and to explore any short time variability. However, for the majority of SPLOT we opted for a single snapshots to fit our initial aims of exploring as large a volume of the polarimetric parameter space, discussed in Section 2.1, as possible.

5.5.4 Highlighting sources of astrophysical interest

The sample contains some sources that belong to rare subclasses and, as such, even a single polarization data point is of astrophysical interest and helps to fill out blanks in the parameter space sketched in Fig. 1. We highlight a few interesting sources below but for a full discussion on all individual sources see the online appendix.

Gaia16aok: Gaia16aok discovered as an outburst from a previously quiescent source with observed radio emission, exhibited very high levels of polarization – $P = 11.51(\pm0.07)$ per cent in V-band. A source with these properties coupled with an unknown progenitor warrants further follow-up observations to uncover the underlying physical mechanism.

Gaia17bvo: Gaia17bvo a galactic variable with no previous classification also exhibited significant polarization. We measured a polarization of $P = 8.37(\pm0.37)$ per cent in Z-band. As in the case of Gaia16aok, the single-snapshot polarimetric observation highlights the potential interest in this source.

OGLE16aaa: we observed OGLE16aaa, a Tidal Disruption Event (TDE) with a V-band polarization of $P = 1.81(\pm0.42)$ per cent – lower than previous measurements of relativistic TDEs and one of only a handful of TDE polarimetric observations (Wiersema et al. 2012a; Wiersema et al., in preparation) .

P13 NGC 7793: we measured a polarization of $P < 6.54$ per cent from the V band observation of P13 NGC 7793, a pulsating Ultra-luminous X-ray Source (ULX) with a period of ∼0.42 s comprising of a black hole and a donor star. This is the first polarization measurement of a ULX but ideally under better weather conditions this limit would have been more constraining. A strongly beamed jet could lead to strongly polarized optical light in some ULXs.

5.6 Looking to the future

The real test looking forward is if a survey like SPLOT can detect sources of astrophysical interest within the stream of alerts through its polarimetry alone, even for sources without prior spectroscopic classification. This ability will be greatly increased by targeting a more homogeneous set of transients (e.g. coming from one, well-defined, stream-like ZTF) on nights less affected by weather. For a future, more mature, imaging polarimetry survey an algorithmic target selection process could be implemented using one of these transient streams and would likely result in a higher science return for the sample as a whole, by allowing proper statistics. Limits could be placed on the age of the transient to get a higher scientific return for transients where the time-scale of polarimetric change is similar to the time since first source detection, though case should be taken to scan the full polarimetric parameter space, especially for sources with ambiguous or unknown classification.

The SPLOT survey was conducted during Visitor nights, with a visiting observer (KW + AH for EFOSC2, KW for SofI) at the observatory as the NTT is run almost entirely in Visitor mode. A service mode operated programme or robotic telescope would give a larger yield of transients for future surveys, a better ability to deal with changing conditions and a better ability to target rarer classes of transient. However, future larger volume transient feeds may negate some of the above points. During the SPLOT runs, we always had available transients to observe, even in periods of strict pointing and poor weather and the ePESSTO project has shown that transient programmes can be run well in Visitor mode. In a future survey, our SPLOT-like survey results can all be disseminated via ATels (i.e. Higgins & Wiersema 2016; Wiersema & Higgins 2016) or using rapid automated channels (e.g. VOEvent) so that they can be linked to alerts via a broker-like ANTARES[15] (Saha et al. 2016), which annotates alerts with radio to X-ray catalogue information, as well as time-domain information, on short time-scales.

6 CONCLUSIONS

We undertook our SPLOT survey to test the feasibility of using linear optical polarimetry as a tool to both add value to large transient data streams and to highlight objects of potential scientific interest, in near real time. We obtained polarimetric measurements of ∼50 optical transients including OGLE16aaa, a TDE and P13 NGC 7793, a pulsating ULX – where the number of previous polarimetric observations of these transient classes is very limited. We also observed a number of previously unclassified transients, some of which exhibited high levels of polarization and significant variability in brightness (i.e. Gaia16alw and Gaia16aok). In addition, we have produced a calibration method that successfully removes instrumental polarization effects for both EFOSC2 and SOFI. This resulted in the creation of software that allows semi-automated reduction, analysis and calibration of incoming imaging polarimetry data fast enough that dissemination of results can be done within hours of data taking.

With the advent of much larger transient missions mapping out huge volumes of transient parameter space, SPLOT has demon-

[15] https://www.noao.edu/ANTARES

strated that similar polarimetric surveys would be a welcome addition in highlighting sources for further follow-up. In combination with rapid radio and X-ray data, polarization can provide a fast way to aid in selection of transients for studying of astrophysical sources non-thermal emission processes and increase the exploration of this vast multidimensional parameter space.

ACKNOWLEDGEMENTS

We thank the anonymous referee for their constructive report that improved this paper. Based on observations collected at the European Organisation for Astronomical Research in the Southern Hemisphere under ESO programme 097.D-0891(A) and 099.D-0262(A). This research made use of data from the Steward Observatory spectropolarimetric monitoring project which is supported by Fermi Guest Investigator grants NNX08AW56G, NNX09AU10G, NNX12AO93G, and NNX15AU81G. This work has also made use of data from the European Space Agency (ESA) mission *Gaia* (https://www.cosmos.esa.int/gaia), processed by the *Gaia* Data Processing and Analysis Consortium (DPAC, https://www.cosmos.esa.int/web/gaia/dpac/consortium) and the *Gaia*, DPAC and the Photometric Science Alerts Team (http://gsaweb.ast.cam.ac.uk/alerts). Funding for the DPAC has been provided by national institutions, in particular the institutions participating in the *Gaia* Multilateral Agreement. ABH is supported by a Science and Technology Facilities Council (STFC) studentship granted by the University of Leicester. KW, RLCS, and NRT acknowledge support from STFC. RLCS acknowledges support from Royal Society Research Grant RG170230. HFS is supported by a PhD studentship granted by the University of Sheffield. ŁW acknowledges the Polish National Science Centre (NCN) grant OPUS 2015/17/B/ST9/03167. We are grateful to all ESO support staff at La Silla, for their assistance and encouragement and we particularly thank Ivo Saviane for allowing us to use SofI when EFOSC2 was unusable. We thank Cristina Baglio for her kind assistance with SofI OBs. KW thanks Dipali Thanki and Ray McErlean for their excellent support of science operations at the University of Leicester observatory (UL50). This research made extensive use of the app *iObserve*, written by C. Foellmi (https://onekilopars.ec). We are grateful to Dr Foellmi for his commitment to this app. This research made use of ASTROPY, a community-developed core PYTHON package for Astronomy (Astropy Collaboration et al. 2018). We acknowledge ESA *Gaia*, DPAC, and the Photometric Science Alerts Team (http://gsaweb.ast.cam.ac.uk/alerts). We thank S. Zane and E. Rol for their contributions to the paper. We thank the cooks at La Silla observatory for their crucial work .

REFERENCES

Astropy Collaboration et al., 2018, AJ, 156, 123
Bertin E., Arnouts S., 1996, A&AS, 117, 393
Buzzoni B. et al., 1984, The Messenger, 38, 9
Chambers K. C. et al., 2016, preprint (arXiv:1612.05560)
Chandrasekhar S., 1960, Radiative Transfer. Dover, New York
Cikota A., Patat F., Cikota S., Faran T., 2017, MNRAS, 464, 4146
Covino S., Gotz D., 2016, Astron. Astrophys. Trans., 29, 205
Covino S. et al., 2014, Astron. Nachr., 335, 117
Covino S. et al., 2017, Nat. Astron., 1, 791
de Serego Alighieri S., 2017, Exp. Astron., 43, 19
ESO, 2016a, EFOSC2 User Manual issue 4.1; LSO-MAN-ESO-361000-0004. European Southern Observatory
ESO, 2016b, SofI User Manual issue 2.4; LSO-MAN-ESO-401000-0004. European Southern Observatory
Evans A., Yudin R. V., Naylor T., Ringwald F. A., Koch Miramond L., 2002, A&A, 384, 504
Foreman-Mackey D., Hogg D. W., Lang D., Goodman J., 2013, PASP, 125, 306
Gaia Collaboration et al., 2016, A&A, 595, A1
Giro E., Bonoli C., Leone F., Molinari E., Pernechele C., Zacchei A., 2003, in Fineschi S., ed., Proc. SPIE Vol. 4843, Polarimetry in Astronomy. p. 456
Higgins A. B., Wiersema K., 2016, Astron. Telegram, 9179
Ivezic Z. et al., 2008, Serb. Astron. J., 176, 1
Janesick J. R., 2001, Scientific Charge-Coupled Devices. SPIE Optical Engineering Press, Bellingham, WA
Kawabata K. S. et al., 2014, ApJ, 795, L4
Keller S. C. et al., 2007, PASA, 24, 1
Kulkarni S. R., 2016, in American Astronomical Society Meeting Abstracts. p. 314.01
Lindegren L. et al., 2018, A&A, 616, A2
Lipunov V. M. et al., 2004, Astron. Nachr., 325, 580
LSST Science Collaboration et al., 2009, preprint (arXiv:0912.0201)
Magalhaẽs A. M. et al., 2012, in Hoffman J. L., Bjorkman J., Whitney B., eds, AIP Conf. Ser. Vol. 1429, Stellar Polarimetry: From Birth to Death. Am. Inst. Phys., New Yorkp. 244
Maund J. R., Wheeler J. C., Baade D., Patat F., Höflich P., Wang L., Clocchiatti A., 2009, ApJ, 705, 1139
Moorwood A., Cuby J.-G., Lidman C., 1998, The Messenger, 91, 9
Patat F., Romaniello M., 2006, PASP, 118, 146
Plaszczynski S., Montier L., Levrier F., Tristram M., 2014, MNRAS, 439, 4048
Quinn J. L., 2012, A&A, 538, A65
Rakic A. D., Djurisic A. B., Elazar J. M., Majewski M. L., 1998, Appl. Opt., 37, 5271
Rau A. et al., 2009, PASP, 121, 1334
Reilly E., Maund J. R., Baade D., Wheeler J. C., Höflich P., Spyromilio J., Patat F., Wang L., 2017, MNRAS, 470, 1491
Rice S. O., 1944, Bell Systems Tech. J., 23, 282
Rol E. et al., 2003, A&A, 405, L23
Russell D. M., Fender R. P., 2008, MNRAS, 387, 713
Saha A. et al., 2016, Proc. SPIE, 9910, p. 99100F
Sajina A., Partridge B., Evans T., Stefl S., Vechik N., Myers S., Dicker S., Korngut P., 2011, ApJ, 732, 45
Serkowski K., 1958, Acta Astron., 8, 135
Serkowski K., Mathewson D. S., Ford V. L., 1975, ApJ, 196, 261
Shapiro P. R., Sutherland P. G., 1982, ApJ, 263, 902
Shappee B. et al., 2014, in American Astronomical Society Meeting Abstracts #223. p. 236.03
Simmons J. F. L., Stewart B. G., 1985, A&A, 142, 100
Smartt S. J. et al., 2015, A&A, 579, A40
Stenflo J. O., 1994, Instrumentation for Solar Polarimetry. Springer Netherlands, Dordrecht, p. 312
Stevance H. F. et al., 2017, MNRAS, 469, 1897
Swinbank J., 2014, Astron. Comput., 7, 12
Trippe S., 2014, J. Korean Astron. Soc., 47, 15
Wang L., Wheeler J. C., 2008, ARA&A, 46, 433
Wang L., Wheeler J. C., Li Z., Clocchiatti A., 1996, ApJ, 467, 435
Wang L., Wheeler J. C., Höflich P., 1997, ApJ, 476, L27
Wardle J. F. C., Kronberg P. P., 1974, ApJ, 194, 249
Wiersema K., Higgins A. B., 2016, Astron. Telegram, 9181
Wiersema K. et al., 2012a, MNRAS, 421, 1942
Wiersema K. et al., 2012b, MNRAS, 426, 2
Wiersema K. et al., 2014, Nature, 509, 201
Wiersema K., Higgins A. B., Covino S., Starling R. L. C., 2018, PASA, 35, e012
Wyrzykowski Ł. et al., 2014, Acta Astron., 64, 197
Zaroubi S. et al., 2015, MNRAS, 454, L46
Zelaya P. et al., 2017, ApJ, 836, 88

SUPPORTING INFORMATION

Supplementary data are available at *MNRAS* online.

Appendix A. Observations of unpolarized standard stars with SofI.

Appendix B. Individual source results.

Please note: Oxford University Press is not responsible for the content or functionality of any supporting materials supplied by the authors. Any queries (other than missing material) should be directed to the corresponding author for the article.

This paper has been typeset from a TEX/LATEX file prepared by the author.